Supporting Information

Capillary Wicking in Hierarchically Textured Copper Nanowire Arrays

Jonggyu Lee[1], Youngjoon Suh[1], Pranav P. Dubey[1], Michael T. Barako[1,2], Yoonjin Won[1,]*

[1] Department of Mechanical and Aerospace Engineering, University of California, Irvine, Irvine, CA, 92697, USA.

[2] NG Next, Northrop Grumman Corporation, Redondo Beach, CA, 90278, USA.

KEYWORDS. nanowires, surface modification, wickability, capillary, flexible electronics

SI 1. Surface characterization of the CuO nanocactuses

This section presents the wetting property and surface characterization as a function of surface modification. First, the copper oxide layer in alkaline solution is developed on the outer surface as shown in Figure S1a, and the corresponding wettability is measured in Figure S1b. The surface becomes hydrophilic in the early stage of the oxidization process of 20 secs, confirming that a short period of oxidization is enough to make hierarchical structures hydrophilic. The droplets dynamics are further analyzed in Figure S4 to show the semi-wicking behavior.

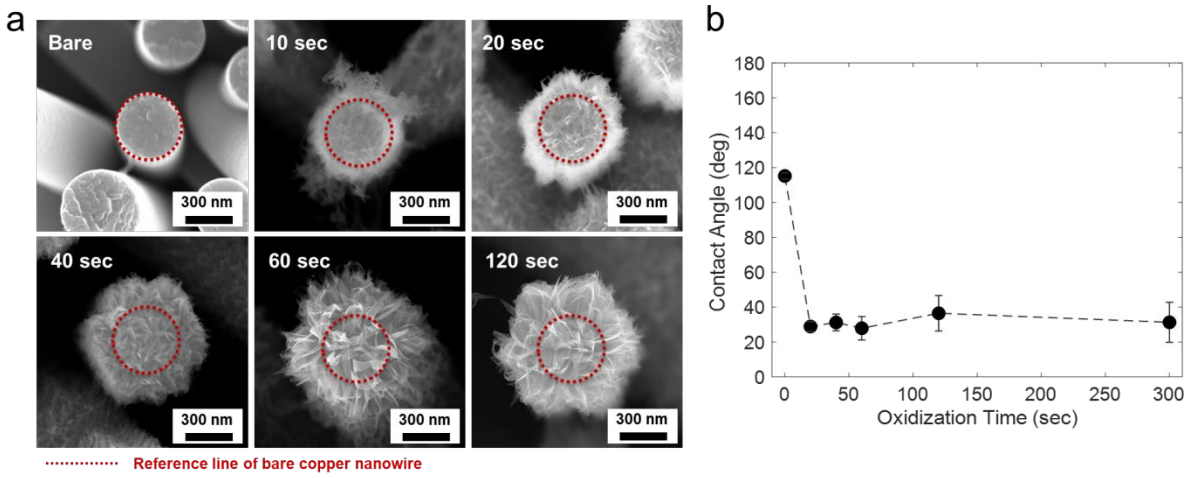

Figure S1. Surface morphology and wetting property for varying oxidation time. (a) SEM images show the increase in CuO nanocactuses diameters depending on the oxidization time. The copper oxide layer in alkaline solution is developed on the outer surface. The nanocactus diameter increases until 60 sec and get stabilized. The red dash line represents the reference line of the initial bare nanowires' diameter. (b) Contact angle results show that the CuO nanocactuses become hydrophilic after 20 sec of oxidization, and the contact angle remains a constant regardless of the oxidization time.

The surface composition is characterized by X-ray diffraction (XRD), and X-ray photoelectron spectroscopy (XPS). The result of XRD in Figure S2 identifies the surface composition after the oxidization. In addition, the surface composition change from the Cu_2O to CuO is demonstrated by performing the ion-etching XPS method, as shown in Figure S3.

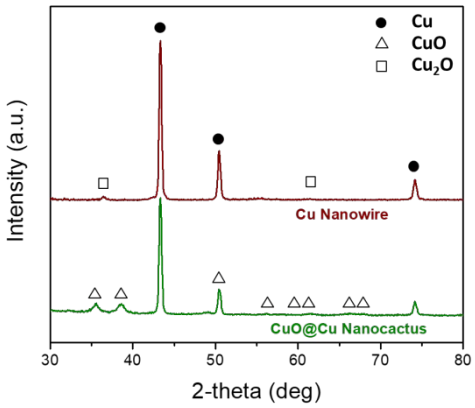

Figure S2. X-ray diffraction (XRD) measurement to characterize surface composition before and after oxidization. The Cu nanowires (brown) show both Cu peak and Cu_2O peak due to the presence of the native copper oxide layer while the CuO nanocactuses (green) show CuO peaks after surface oxidization.

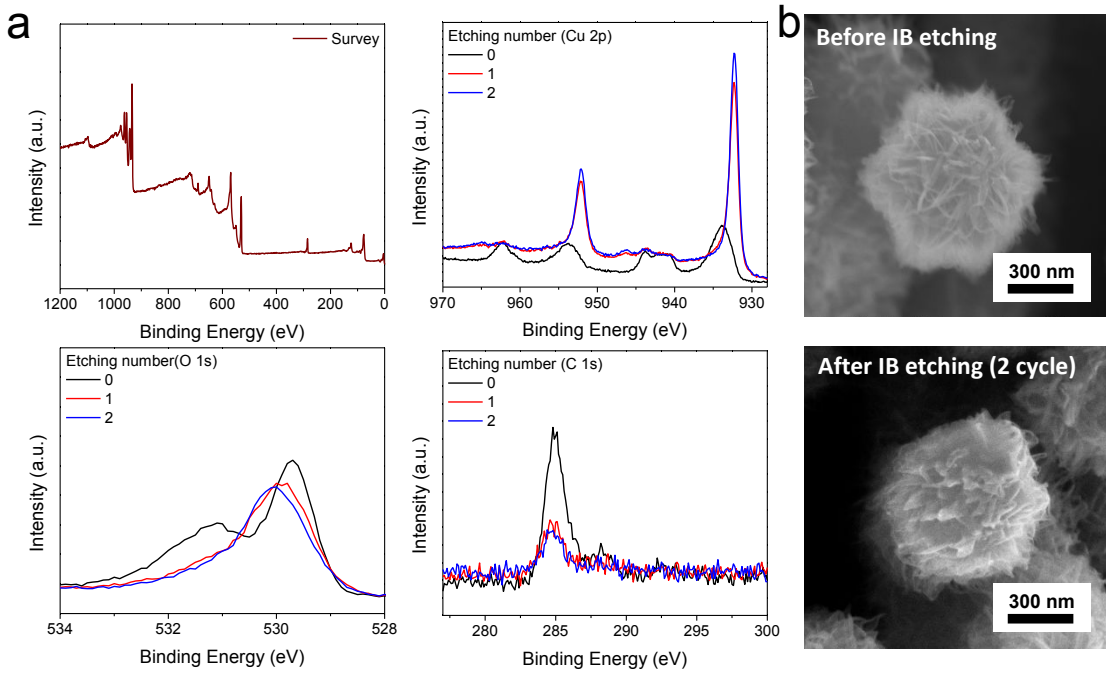

Figure S3. (a) X-ray photoelectron spectroscopy (XPS) measurement using ion beam etching technique. The survey result shows that the surface is mainly composed of copper, oxygen, and carbon. The Cu 2p peak before etching shows CuO peak at first and after etching the peak shows Cu_2O, which agrees with the previous results of copper oxidization. In addition, O 1s peak confirms the surface composition of the oxide layer. C 1s peak shows impurities on the surface, but the intensity of the impurities is negligible at the survey peak. (b) The SEM images show the before and after ion beam (IB) etching of the CuO nanocactuses.

The surface morphology is analyzed considering the hierarchically textured surface to define the surface roughness and porosity. The areal lost due to the nanowires in contact is calculated based on the image analysis as shown in Figure S4. Nanowire diameter considering textured surface is analyzed in Figure S5 to define the porosity. Also, the roughness without considering the textured surface is shown in Figure S7 to calculate the critical contact angle, $\theta_c = cos^{-1}(1-\varepsilon)/(r-\varepsilon)$.

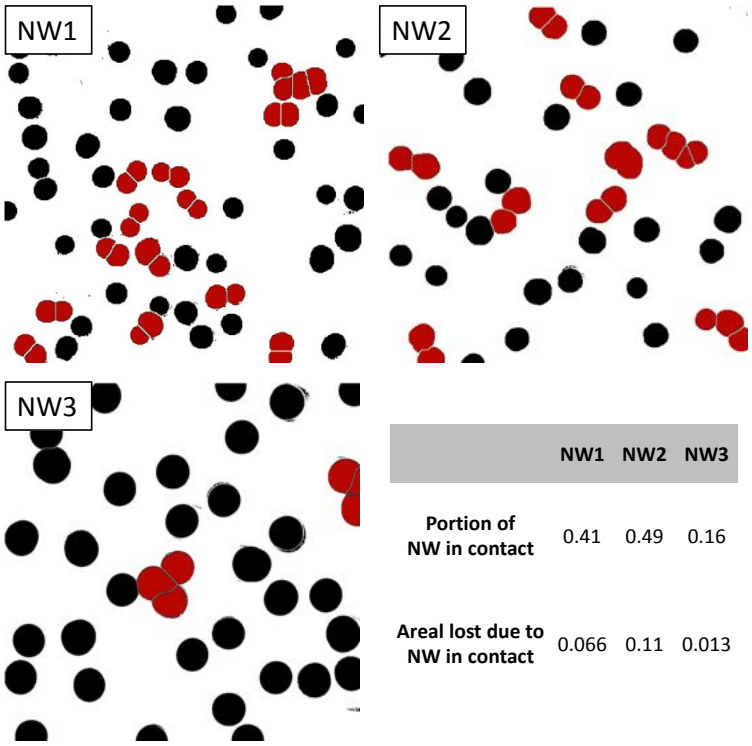

	NW1	NW2	NW3
Portion of NW in contact	0.41	0.49	0.16
Areal lost due to NW in contact	0.066	0.11	0.013

Figure S4. Post-processed SEM images showing nanowire tips (NW1, NW2, and NW3). Each dot represents the nanowire tip, which allows us to identify the nanowires in contact (red dots) and calculate the areal lost due to the contacts. The areal lost for each set is 2.7%, 5.4%, and 0.2% for NW1, NW2, and NW3, respectively.

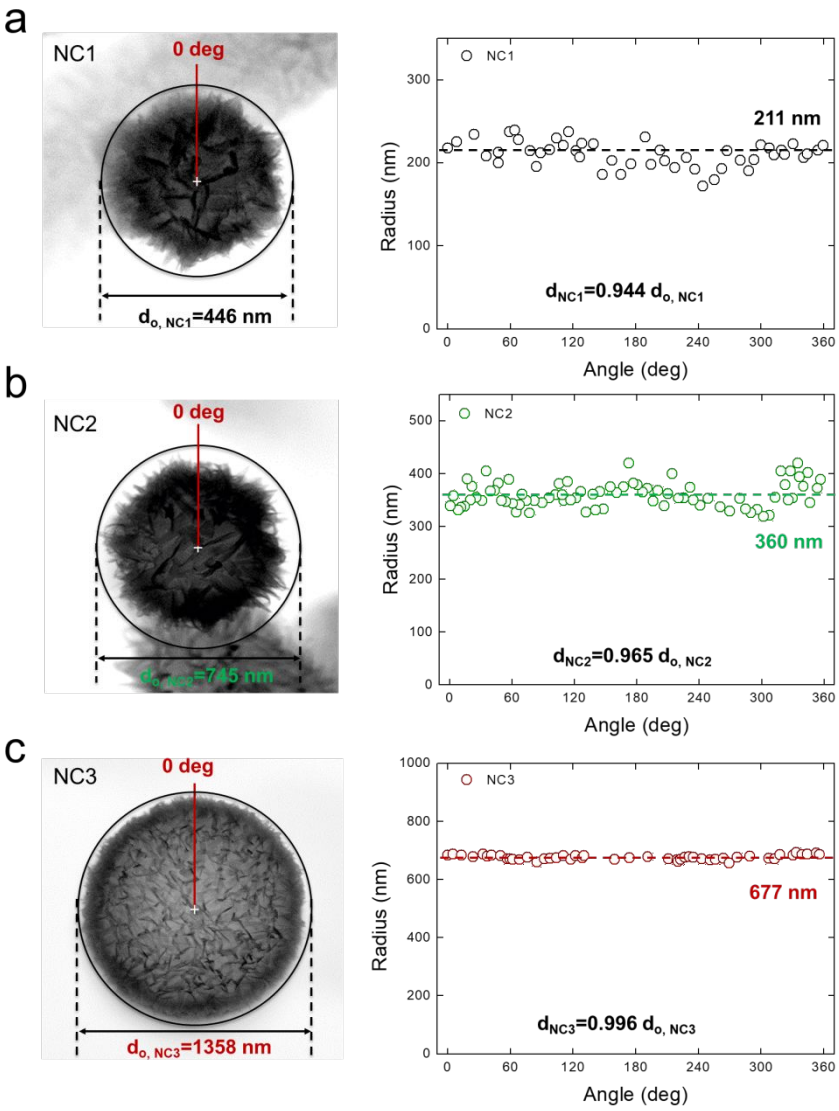

Figure S5. SEM images and plots showing the diameter analysis of an individual nanocactus after oxidization. The SEMs show the outer diameter d_o of an individual nanowire from (a) NC1, (b) NC2, and (c) NC3. Then, the apparent diameter is analyzed by measuring the angle-dependent radius, allowing us to calculate the average diameter as well as overall porosity. The average diameter can be expressed as $d = Ad_o$, where the coefficients A are 0.944, 0.965, and 0.996 for NC1, NC2, and NC3, respectively.

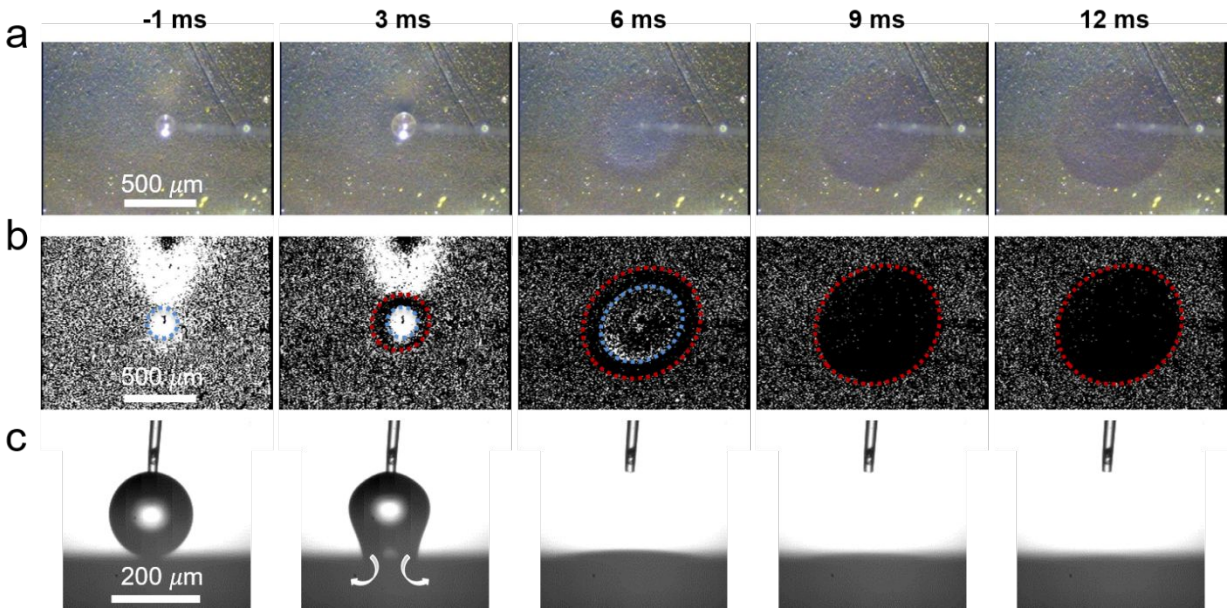

Figure S6. The radial liquid spreading behavior on the NC2 surface with optical microscope images from (a-b) top and (c) side view. (a-b) The optical microscope images are processed using ImageJ to identify the boundary of the liquid and wicking front. The red dash line represents the wicking front, and blue dash line represents the liquid meniscus front. Once the droplet touches the surface, wicking begins first before the liquid spreads, called the hemi-spreading or hemi-wicking.[1] This can be explained by the transition from Wenzel state to the liquid film state. Thereby, the resulting droplets show a quick decrease in the contact angle and the droplet volume.

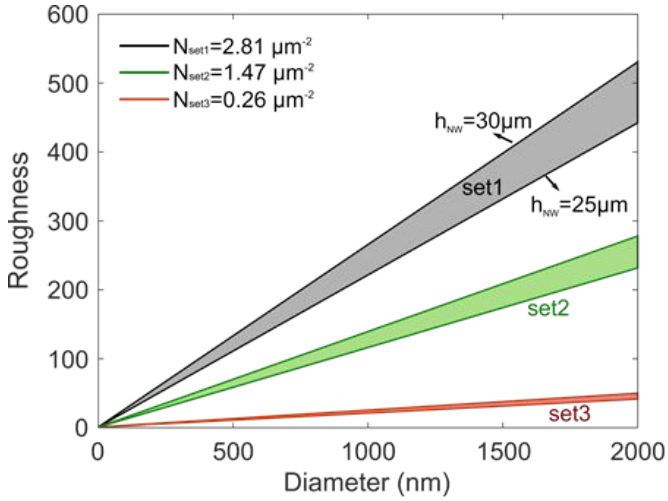

Figure S7. Roughness for different nanowire arrays. The surface roughness $r = 1 + 2\pi d\, h_{NW}/\sqrt{3}p^2$ is directly proportional to the diameter with a constant number density or a pitch. The roughness is calculated based on the nanowire height ranging from 25 μm to 30 μm because a membrane height 30 μm is used.

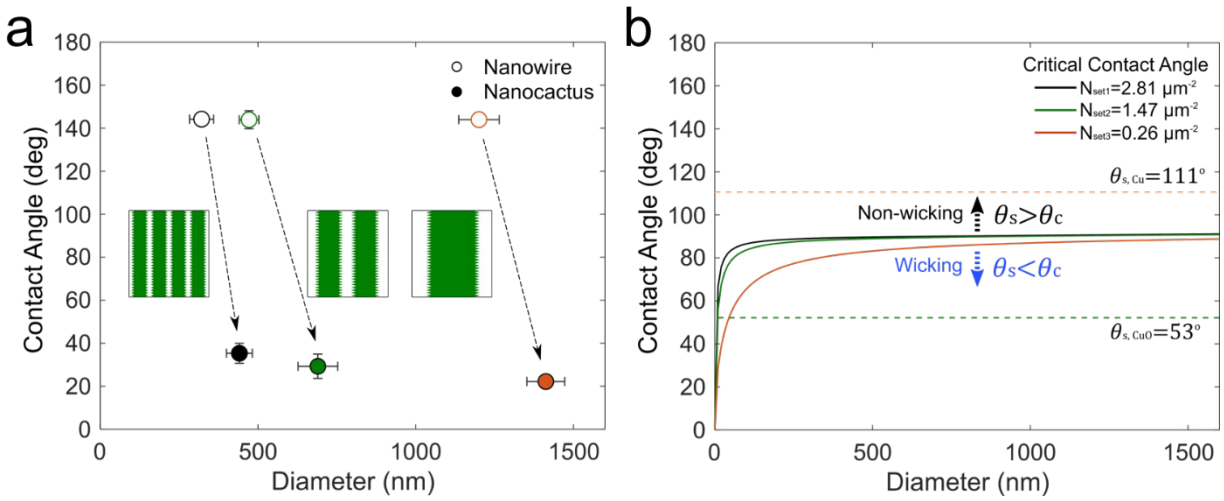

Figure S8. Contact angle and theoretical calculation of critical contact angle of the nanowire arrays for each number density. (a) Contact angle measurements show that hydrophobic Cu nanowires become hydrophilic CuO nanocactuses after surface texturing and oxidation. The error bars indicate the standard deviation of diameter and contact

angle. (b) The critical contact angle shows a potential of the nanocactuses for wicking. Once the static contact angle is lower than critical contact angle, the porous surface favors capillary wicking. The critical contact angle plot is calculated based on the roughness shown in Figure S5. The static contact angles of Cu substrate and CuO textured substrate are 111° and 53°, respectively.

SI 2. Capillary Rise Theory and Capillary Performance Parameter.

The capillary pressure through the porous media is dictated by the surface tension of the liquid and interfacial interaction between liquid-vapor. The relation of the capillary pressure P_{cap} can be expressed with the Laplace-Young equation:

$$\Delta P_{cap} = \frac{2\sigma \cos\theta_s}{R_p} \tag{S1}$$

where σ is the surface tension of the liquid, and R_p is the static pore radius. During the wicking process, the capillary pressure should be equal to the summation of the viscous friction, gravity, and evaporation for momentum balance as given by[2]:

$$\frac{2\sigma cos\theta_s}{R_p} = \frac{\phi}{K}\mu hv + \frac{\dot{m}_{evp}\mu}{2d_{film}\rho K}h^2 + \rho gh \tag{S2}$$

where K is permeability, μ is the liquid viscosity, d_{film} is film thickness, and ρ is the liquid density. The mass evaporation rate $\dot{m}_{evp}$ is assumed to be zero in the vapor saturation condition in the chamber. The gravitational term including the gravitational acceleration g is negligible in the condition of such a low wicking height (< 10 mm) at the permeability over 1×10^{-20} m^2. Therefore, the eq (S2) can be reduced to the Lucas-Washburn equation[3,4]:

$$h^2 = \frac{4\sigma \ K}{\phi\mu R_{eff}}t \tag{S3}$$

where the effective radius $R_{eff} = R_p/\cos\theta_s$.

SI 3. Permeability calculation using numerical simulation

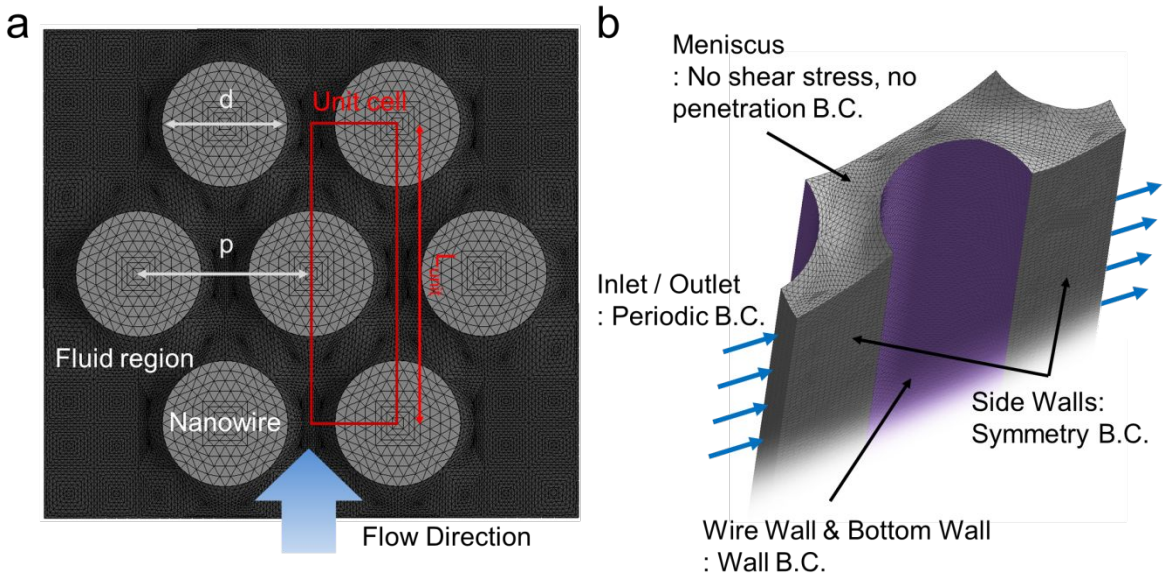

Figure S9. (a) Schematic illustration of the hexagonally aligned nanowires and (b) boundary conditions for the numerical simulation.

We predict the permeability K of the nanowire structures using numerical simulations and compare it with experimental data. The static liquid free surface shapes in the nanowire structures are first predicted based on surface energy minimization algorithms by utilizing Surface Evolver. The estimated meniscus shape is post-processed with a commercial CAD design package and imported to ANSYS Fluent for computer fluid dynamics (CFD) calculations. Figure S8a and b show the unit cell and the boundary conditions for the fluidic unit cell, where p is the distance between the center of the nanowires, and d is the nanowire diameter. We apply periodic pressure boundary conditions to ensure that the velocity profile is equal at the inlet and outlet. In this paper, we assume that the shear stress on the liquid meniscus is negligible because the viscosity of air is considerably smaller than that of water. A symmetry boundary condition is applied to the side walls. The simulation models employ SIMPLE scheme for pressure linked equations, PRESTO! scheme for pressure discretization, and least square cell-based formulation for gradient spatial discretization. The predicted average velocity difference between the inlet and outlet are used to calculate the permeability by using the Darcy's law:

$$Q = \frac{(KA)\Delta P}{\mu L_{unit}} \quad \text{(S4)}$$

where K is the permeability, A is the cross-sectional area of the formation, μ is the viscosity of the fluid, Q is the flowrate, ΔP is the pressure gradient, and L_{unit} is the traveling length of the system.

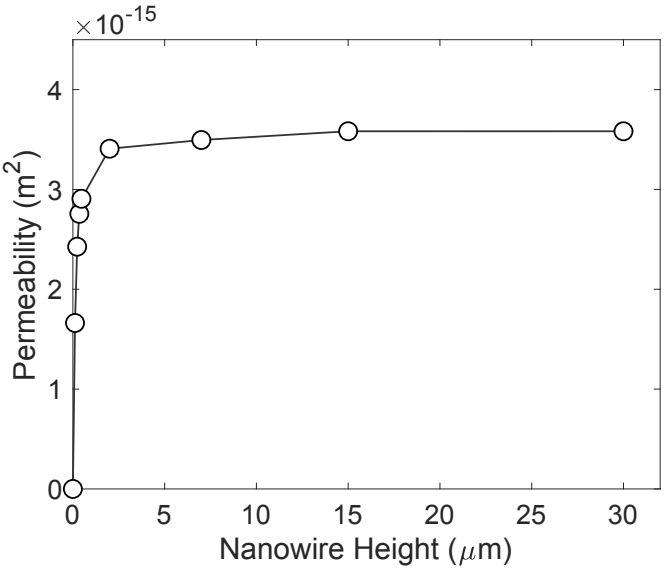

Figure S10. Permeability calculation with various nanowire heights.

We also study the influence of nanowire height h_{NW} on the permeability by calculating simulation models for various nanowire heights. We calculate the nanowires' permeability with a pitch of p = 0.64 μm, a diameter of d = 467.1 nm, and heights varying from 116.7 nm to 30 μm. The permeability rapidly increases when nanowire structure shows a low aspect ratio. The sudden change is attributed to the viscous forces exerted by the bottom surface. Therefore, the diminishing influence of the viscous force due to the increase in the aspect ratio results in constant permeability regardless of nanowire height. The permeability results show a matching trend with the previous studies.[5]

SI 4. Hydraulic diameter D_h calculation of static and freestanding nanocactuses

We define the concept of hydraulic diameter $D_h = 4A/P$, where A is cross-sectional area, P is perimeter, $R_{eff} = D_h/2\cos\theta_s$, and θ_s = 53°. As the liquid pathways vary along the liquid propagation direction, the integration over the quarter of unit cell length ($L_{unit}/4$) is used:

$$D_h = \frac{2}{L}\left(\int_0^{d/2} \frac{Xh_{NW}}{(X + h_{NW})}dy + \int_{d/2}^{L} \frac{Xh_{NW}}{(X + h_{NW})}dy\right) \quad \text{(S5)}$$

where X is defined as

$$X = \begin{cases} p - d\cos\left(\text{asin}\left(\frac{2y}{d}\right)\right) & 0 \le y < d/2 \\ p & d/2 \le y < L \end{cases} \quad \text{(S6)}$$

Also, see Figure S9 for the details of the unit cell length and cross-sectional area. Then, the hydraulic diameter D_h of freestanding nanocactuses with curvature is calculated by eq (4) with changing pitch at the top layer of arrays as shown in Figure S11. The pitch at the bottom remains a constant because the bottom layer is connected to the substrate while the pitch at top layer changes with curvature:

$$X = \begin{cases} p - d\cos\left(\text{asin}\left(\frac{2y}{d}\right)\right) + 0.5a & 0 \le y < d/2 \\ p + 0.5a & d/2 \le y < L \end{cases} \quad \text{(S7)}$$

where $a = \kappa h_{NW} X$ determined by ratio of R_c to h_{NW}. Despite the highly curved state at the macroscale (Figure 7a-b), the alignment changes at the microscale (Figure 7c) are negligible, as represented by the changes in the hydraulic diameter D_h of 0.58% at κ = ±0.11, 0.64% at κ = ±0.15, and 0.71% at κ = ±0.21 mm^{-1}.

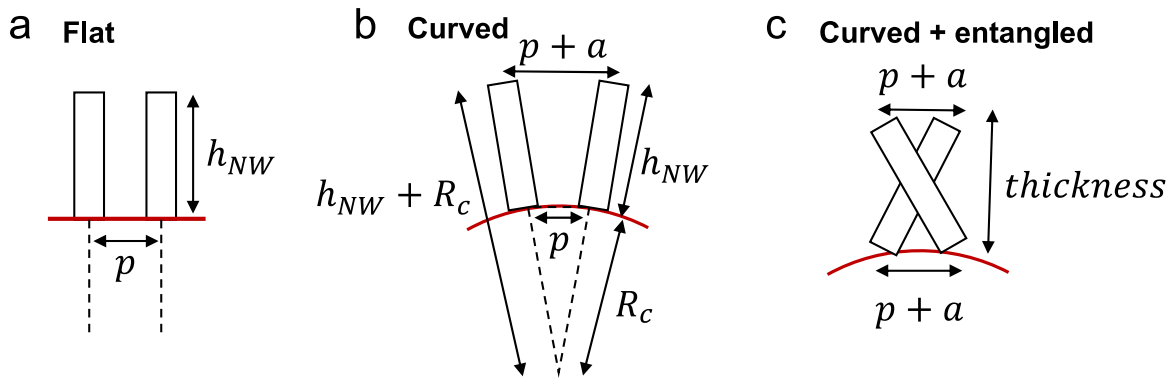

Figure S11. Schematic of the cross-sectional static and freestanding nanowire arrays showing the distance change during bending process. Each illustration shows ideal nanowire arrays on (a) flat, (b) curved, and (c) entangled nanowire arrays on curved surface.

SI 5. Morphology characterization of the flexible nanowire arrays.

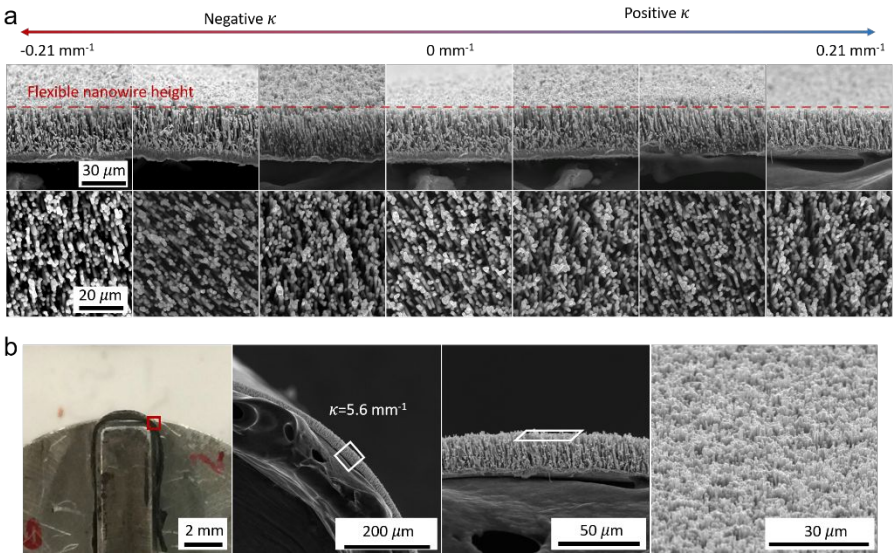

Figure S12. SEM images and photograph of the flexible freestanding nanowires with various curvature. (a) SEM images show the cross-sectional and top view morphology of the freestanding nanowire arrays during bending where the κ = 0, ±0.11, ±0.15, and ±0.21. The changes in nanowire alignments and thickness can be negligible. (b) The photograph and corresponding SEM images show the freestanding nanowires at an extreme bending with κ = 5.6mm^{-1}, confirming the nanowire alignments.

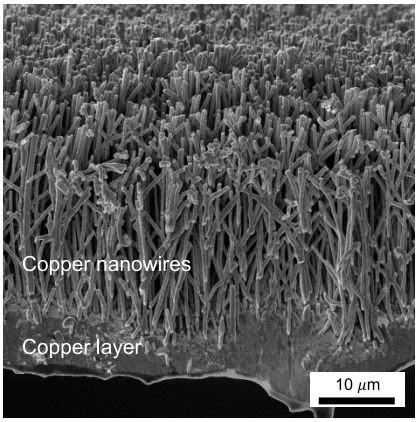

Figure S13. A cross-sectional SEM image of the freestanding nanowire arrays on thin and flexible copper layer. The interface between the nanowires and the substrate is rough due to the direct deposition on the polycarbonate membrane.

SI 6. Wicking measurement setup in a saturated chamber

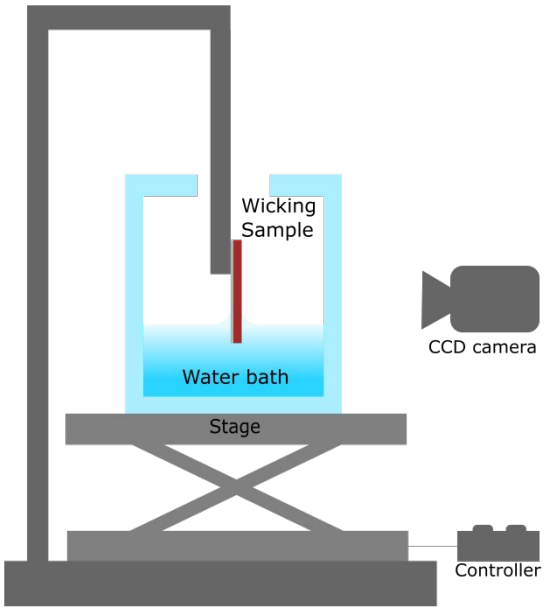

Figure S14. Schematic diagram of the wicking measurement setup. The setup is composed of the liquid chamber, CCD camera, motorized stage, and wicking sample. The motorized stage controls the height of the stage to locate the sample. The chamber is fully closed for a week to set the chamber saturated by water to minimize the evaporation during the wicking test.

SI 7. Uncertainty analysis

Porosity. The porosity is calculated by the number density *N* and diameter *d* of the nanowire arrays. The number density is calculated by counting the number of nanowires with large area (15 μm × 15 μm). Since the counted nanowire number is large enough (> 200) for the set 1 and set 2, the uncertainty associated with number density is considered to be negligible in the porosity calculation. Instead, the uncertainty in the diameter is identified based on the diameter distribution of each sample group (Table 1). Therefore, the uncertainty in the porosity is

$$\left(\frac{\Delta\phi}{\phi}\right)^2 = \left(2\frac{\Delta d}{d}\right)^2 + \left(\frac{\Delta N}{N}\right)^2 \quad \text{(S8)}$$

Capillary performance parameter. Based on the eq (3), the capillary performance parameter is a function of porosity, fluid viscosity, surface tension, wicking height, and measurement time. The uncertainty in the capillary performance parameter is given by

$$\left(\frac{\Delta K/R_{eff}}{K/R_{eff}}\right)^2 = \left(\frac{\Delta\sigma}{\sigma}\right)^2 + \left(\frac{\Delta\phi}{\phi}\right)^2 + \left(\frac{\Delta\mu}{\mu}\right)^2 + \left(2\frac{\Delta h}{h}\right)^2 + \left(\frac{\Delta t}{t}\right)^2 \quad \text{(S9)}$$

The fluid properties vary with the lab temperature 298 ± 2 K; therefore, the uncertainty in the surface tension and viscosity is 0.6% and 4.4%, respectively, which can be negligible. Also, the time frame of the camera is 60 fps, leading to the uncertainty around 8.4 ms, which can be negligible (< 0.015%) over the long measurement period. Therefore, the standard deviation of the wicking height is considered Δh to calculate the overall uncertainty.

Capillary performance parameter of the freestanding nanowire arrays. The uncertainty of the capillary performance parameter of the freestanding nanowire arrays on flexible substrates is

$$\left(\frac{\Delta K/R_{eff}}{K/R_{eff}}\right)^2_{curved} = \left(\frac{\Delta K/R_{eff}}{K/R_{eff}}\right)^2 + \left(\frac{\Delta\kappa}{\kappa}\right)^2 \quad \text{(S10)}$$

with the consideration of the deviations in the curvature.

ABBREVIATIONS

A	cross-sectional area, m^2
d	nanowire or nanocactus diameter, m
D	wicking coefficient, m^2/s
D_h	hydraulic diameter, m
g	gravitational acceleration, m/s^2
h	wicking height, m
h_{NW}	nanowire height, m
K	permeability, m^2
N	number density, um^{-2}
P	perimeter, m
p	pitch, m
p_{hex}	average pitch based on hexagonal model, m
$\mathrm{P_{cap}}$	capillary pressure, Pa
r	roughness
R_p	pore radius, m
R_{eff}	effective pore radius, m
κ	curvature, mm^{-1}
μ	kinetic viscosity, Pa s
ρ	density, kg/m^3
ϕ	void fraction, porosity

ε solid fraction

$\dot{m}_{evp}$ mass evaporation rate, kg/s

σ surface tension, N/m

θ_{app} apparent contact angle, °

θ_s static contact angle, °

θ_c critical contact angle, °

REFERENCES

(1) Wemp, C. K.; Carey, V. P. Water Wicking and Droplet Spreading on Randomly Structured Thin Nanoporous Layers. *Langmuir* **2017**, *33* (50), 14513–14525.

(2) Fries, N.; Dreyer, M. The Transition from Inertial to Viscous Flow in Capillary Rise. *J. Colloid Interface Sci.* **2008**, *327* (1), 125–128.

(3) Washburn, E. W. The Dynamics of Capillary Flow. *Phys. Rev.* **1921**, *17* (3), 273–283.

(4) Lucas, R. Ueber Das Zeitgesetz Des Kapillaren Aufstiegs von Flüssigkeiten. *Kolloid-Zeitschrift* **1918**, *23* (1), 15–22.

(5) Jeon, S.; Byon, C. Effect of Meniscus on the Permeability of Mono-Layered and Multi-Layered Packed Spheres. *Appl. Therm. Eng.* **2016**, *107*, 1287–1293.